The X-IFU end-to-end simulations performed for the TES array optimization exercise

Peille, P.[1] ; Wilms, J.[2] ; Brand, T.[2] ; Cobo, B.[3] ; Ceballos, M.T.[3] ; Dauser, T.[2] ; Smith, S.J.[4] ; Barret, D.[1] ; den Herder, J.W.[5]
Piro, L.[6] ; Barcons, X.[3] ; Pointecouteau, E.[1] ; Bandler, S.[4] ; den Hartog, R.[5] ; de Plaa, J.[5]
[1]IRAP, *France* ; [2]Remeis Observatory & ECAP, *Germany* ; [3]IFCA, *Spain* ; [4]GSFC, *United States*
[5]SRON, *The Netherlands* ; [6]INAF, *Italy*

Abstract: The focal plane assembly of the Athena X-ray Integral Field Unit (X-IFU) includes as the baseline an array of ~ 4000 single size calorimeters based on Transition Edge Sensors (TES). Other sensor array configurations could however be considered, combining TES of different properties (e.g. size). In attempting to improve the X-IFU performance in terms of field of view, count rate performance, and even spectral resolution, two alternative TES array configurations to the baseline have been simulated, each combining a small and a large pixel array. With the X-IFU end-to-end simulator, two science cases among those selected by the X-IFU science team as potentially driving the optimal TES array configuration, have been simulated for the results to be scientifically assessed and compared. In this poster, we will describe the simulation set-up for the various array configurations, and highlight some of the results of the test cases simulated.

The TES array optimization exercise

The recent development of mixed Transition Edge Sensor (TES) array configurations combining pixels of different properties (see Poster 12.02) offers the opportunity to investigate improvements of the X-IFU performance in terms of field of view, count rate capability and even spectral resolution. A TES array optimization exercise is therefore currently being conducted by the X-IFU consortium to try to identify the best configuration considering technical constraints.

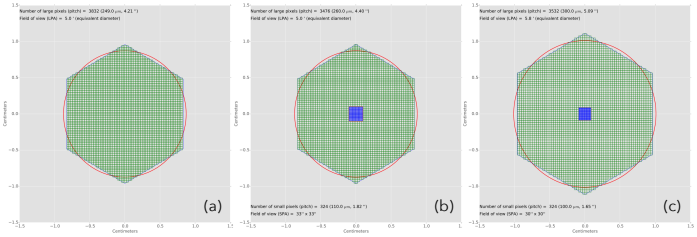

Figure 1: The three TES array configurations considered in the optimization exercise. (a) Baseline single pixel array with 249 µm pixel pitch. 5′ FoV. (b) SPA: 324 small pixels with 110 µm pitch. LPA: 3476 large pixels with 260 µm pixel pitch. 5′ FoV. (c) SPA: 324 small pixels with 100 µm pitch. LPA: 3532 large pixels with 300 µm pixel pitch. 5.8′ FoV.

Apart from the baseline monolithic ~ 4000 pixels array, two additional designs featuring a small pixel array (SPA) and a large pixel array (LPA) were considered: one keeping the baseline 5′ FoV and the other increasing it to 5.8′ at the expense of an increased LPA pixel size. These configurations were elaborated under the constraints of keeping the total number of pixels about constant and retaining the 2.5 eV energy resolution requirement for all pixels.

Development of a detector physical model

A new detector physical model was developed by the X-IFU End-to-End simulations team. It is based on the numerical solving of the differential equations for the time-dependent temperature, *T(t)*, and current, *I(t)*, in the TES:

$$C\frac{dT}{dt} = R(I,T)I^2 - P_{\rm bath} + P_{\rm noise} + P_{\rm Xray} \qquad L\frac{dI}{dt} = V_{\rm bias} - (R(I,T) + R_{\rm load})I + V_{\rm noise}$$

The TES itself is modeled as a resistor linearly dependent on *T* and *I* as parametrized by:

$$\alpha = \frac{T_0}{R_0}\frac{\partial R}{\partial T}\bigg|_{I_0} \qquad \beta = \frac{I_0}{R_0}\frac{\partial R}{\partial I}\bigg|_{T_0}$$

The model also includes the thermal link to the thermal bath. The noise sources included in the model are thermal fluctuations between the TES and the heat bath, electrical Johnson noise of the TES and load resistor, and readout noise from the SQUID and amplifier chain. Also included is an unexplained noise parameter (based on empirical characterization) that represents sources of noise internal to the TES that are as yet not fully understood (Irwin & Hilton, 2005).

The GSFC detector team provided detector parameters for the different TES array configurations (see Table 1). Using those, realistic read-out streams can be simulated as illustrated by Figure 2.

Table 1: Main parameters of the different TES sensors considered for the TES array optimization exercise. One can notably notice how the SPA pixels with their small fall time are optimized for high count rates.

Parameter	LPA (a)	LPA (b)	LPA (c)	SPA (b-c)
Heat capacity, C	0.8 pJ/K	0.8 pJ/K	0.8 pJ/K	0.26 pJ/K
Bath conductance	200 pW/K	115 pW/K	57 pW/K	300 pW/K
Alpha	75	75	75	100
Beta	1.25	1.25	1.25	10
Unexplained noise factor	0	0	0	0.8
Power	4.81 pW	2.76 pW	1.38 pW	5.95 pW
Fall time	404 µs	705 µs	1.41 ms	75 µs
Intrinsic energy resolution	1.68 eV	1.68 eV	1.68 eV	1.53 eV

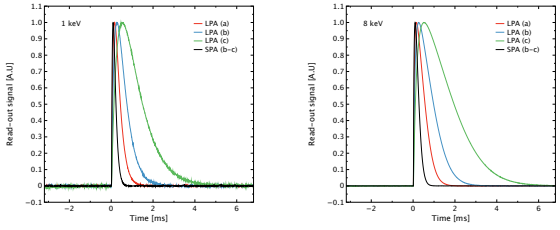

Figure 2: Simulated pulse shapes for an X-ray impact at *t*=0 of energy 1 keV (left) and 8 keV (right). The shapes were scaled to unity for better comparison. The difference in rise and fall time between the detectors is clearly visible depending on whether they are optimized for high count rates (SPA and LPA (a)) or not (LPA (b) and LPA (c)). One can also notice the pulse shape changes with energy due to the detectors non-linearities.

References: Dauser T., Wilms J., Reynolds C.S., Brenneman L.W., 2010, MNRAS 409, 1534
García J., Dauser T., Lohfink A., et al., 2014, ApJ 782, 76
Irwin K. D. and Hilton G. C., 2005, Cryogenic Particle Detection, Topics Appl. Phys. 99, 63-152
Szymkowiak A., Kelley R., Moseley S., Stahle C., 1993, J. Low Temp. Phys. 93, 281

Quantifying each pixel individual performance

To characterize the degradation of energy resolution and bias (mean systematic error on the reconstructed energy) at high count rates, a succession of triplets of 6 keV pulses have been simulated and reconstructed with the Optimal Filtering technique (see Figure 3 ; Szymkowiak et al., 1993). This allows to obtain energy resolution and bias maps of the middle event as a function of the companions time separations for all the different pixels (see Figure 4 and Poster 12.05).

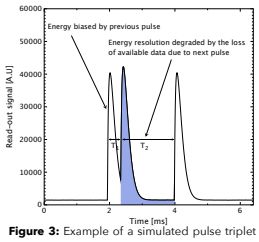

Figure 3: Example of a simulated pulse triplet for an SPA pixel and 6 keV pulses.

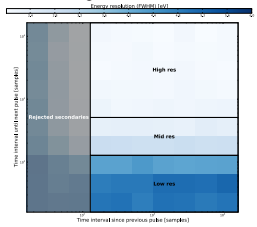

Figure 4: Energy resolution map for the SPA at 6 keV with the event grading definitions.

From these maps, one can derive different event grades that will be affected to each impacting X-ray depending on the closeness of other events and estimate the corresponding energy resolution. Rejected events are those for which the energy bias is larger than 0.2 eV (see rejected secondaries in Figure 4). High resolution events were chosen as those for which there was no significant energy resolution degradation, while medium resolution events feature a final resolution of 3 eV. Low resolution events are the remaining valid events.

Table 2: Event grading definitions and corresponding final energy resolution for all the different pixels

Parameter	LPA (a)	LPA (b)	LPA (c)	SPA (b-c)
Valid event criterium	$T_1 \geq 2.6$ ms	$T_1 \geq 5.1$ ms	$T_1 \geq 9$ ms	$T_1 \geq 820$ µs
High res event criterium / ΔE	$T_2 \geq 6.6$ ms / 2.5 eV	$T_2 \geq 105$ ms / 2.5 eV	$T_2 \geq 105$ ms / 2.5 eV	$T_2 \geq 3.3$ ms / 2.5 eV
Medium res event criterium / ΔE	$T_2 \geq 1.6$ ms / 3.0 eV	$T_2 \geq 3.3$ ms / 3.0 eV	$T_2 \geq 6.6$ ms / 3.0 eV	$T_2 \geq 820$ µs / 3.0 eV
Low res event criterium / ΔE	N/A / 15 eV	N/A / 30 eV	N/A / 90 eV	N/A / 15 eV

Scientific performance of the different TES array configurations

For the purpose of this study, the SIXTE end-to-end simulator (see Posters 12.06 and 12.14) was modified to allow advanced focal plane geometries with pixels of heterogeneous properties. To take into account the above described energy resolution dependence with count rate, within the simulation process, the energy of each photon is randomized depending on its measured grade.

To characterize the X-IFU bright source performance in a general way, we used a standard point-like source with a spectrum corresponding to the Crab nebula and pulsar and varied its intensity. Figure 5 shows the event grades ratios for all the different setups as a function of the count rate.

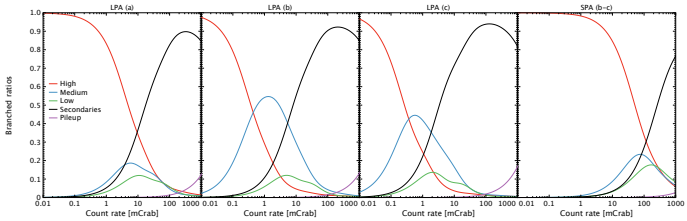

Figure 5: Event grades ratios for all studied configurations as a function of count rate (1 mCrab ≈ 94 cps on the whole sensor array).

All configurations match the 80 % of high resolution events at 1 mCrab requirement
Introducing an SPA further improves the count rate capability by an order of magnitude

To further study the instrument performance at different count rates, black hole spin measurements were simulated using the *relxill* model (Dauser et al., 2010; García et al., 2014) with a spin parameter *a* = 0.99 and an underlying cut-off power law of photon index 1.9. Figure 6 shows how the parameters are reconstructed as a function of count rate for the different TES array setups.

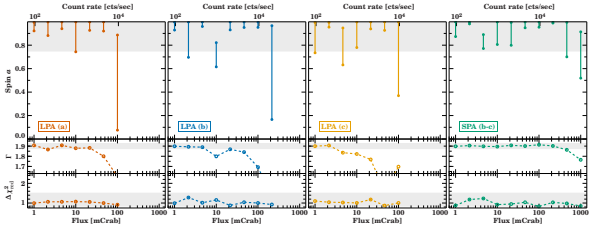

Figure 6: Spin and photon index parameters as reconstructed from simulations at different count rates and for all the TES array configurations. The high, medium, and low resolution spectra were jointly fitted using for each response matrices of the appropriate energy resolution. We note that in all cases 500 000 total source counts (before invalid rejection) were used for comparison purposes. The highlighted bands indicate the expected uncertainties at the 90 % confidence level.

No spectral distortion up to a few 10 mCrab for a monolithic detector
and a few 100 mCrab after introducing an SPA